

Grasso, Marzio, Azzouz, Lyes, Ruiz-Hincapie, Paula, Zarrelli, Mauro and Ren, Guogang (2018) Effect of temperature on the mechanical properties of 3D-printed PLA tensile specimens. *Rapid Prototyping Journal*, 24(8), pp. 1337-1346. ISSN (print) 1355-2546.  
<https://doi.org/10.1108/RPJ-04-2017-0055>

# Effect of Temperature on the Mechanical Properties of 3D-Printed PLA Tensile Specimens

Marzio Grasso, Lyes Azzouz and Paula Ruiz-Hincapie

School of Engineering and Technology, University of Hertfordshire, Hatfield, UK

Mauro Zarrelli

IPCB - Institute of Polymers, Composites and Biomaterials, CNR - Research National Council, Portici, Italy, and

Guogang Ren

School of Engineering and Technology, University of Hertfordshire, Hatfield, UK

## 1. Introduction

Additive manufacturing (AM), also known as “tool-less” manufacturing, can be quickly executed and has progressed substantially in recent years. This technology significantly reduces material waste by eliminating unnecessary processes and assembly steps (Li, Wu et al. 2016). Currently used techniques include fused deposition modelling (FDM), stereo-lithography, selective laser sintering, syringe extrusion and fused filament deposition (FFD) (Gibson, Rosen et al. 2010). FDM is one of the most used 3D printing techniques of thermoplastic polymers. This process is based on the deposition of semi-molten filaments to create an object as a composition of several overlapping layers; of which each layer is composed of filaments laid out according to a predetermined rastering configuration. A significant advantage of utilising FDM technology is the potential to create complex and specific shapes.. The process is currently adopted in bio-engineering, mainly for the manufacturing of tissue engineering scaffolds (Visscher, Bos et al. 2016, Hong, Newman et al. 2017, Shakor, Sanjayan et al. 2017). Additionally, the automotive sector uses this technology to produce small components (Keles, Blevins et al. 2017). However, it is gaining more attention in several other fields including energy harvesting (Bito, Bahr et al. 2017).

Conventionally, fossil fuel based plastics have been widely adopted by several industries. However, over the last several decades eco-friendly, biodegradable and medical grade polymer materials have received considerable attention due to improvements in their manufacturing processes and the possibility of creating blends to achieve more advantageous materials. Among the vast myriad of

45 biodegradable materials, Polylactic Acid (PLA) has emerged as one of the preferred candidates for  
46  
47 3D printing given its many favourable properties including biodegradability, biocompatibility,  
48  
49 composability and recyclability (Farah, Anderson et al. 2016). Additionally, PLA is widely used in  
50  
51 emerging technologies such as 3D printing along with others polymers namely Acrylonitrile  
52  
53 Butadiene Styrene (ABS), PolyCarbonate (PC), and PolyVinyl Alcohol (PVA) (Torres, Coteló et  
54

1  
2  
3 al. 2015). PLA is characterized by low operating temperatures, specifically the glass transition  
4 temperature  $T_g$  and the melting temperature  $T_m$  (Lanzotti, Grasso et al. 2015) which are preferable  
5  
6 characteristic for both the softening during the “deposition” stage ( $T_g$ ) and avoiding localised  
7  
8 degradation process due to hot spot in complex geometry ( $T_m$ ). The fundamental issue in designing  
9  
10 3D printed components is the identification of strength and stiffness (Qin, Compton et al. 2015).  
11  
12 Several authors have carried out experimental tests to investigate the mechanical behaviour. For  
13  
14 instance, in (de Obaldia, Jeong et al. 2015) it is suggested that 3D printed materials exhibit highly  
15  
16 anisotropic behaviour in both their stiffness and strength properties. Other studies have also reported  
17  
18 that an increase in the layer thickness reduces those same features (Durgun and Ertan 2014, Impens  
19  
20 and Urbanic 2016, Torres, Cole et al. 2016). In addition, fracture surface investigations have been  
21  
22 used to explain the high variability in the aforementioned properties; this technique relies on the  
23  
24 identification of physical landmarks that correlate failure mechanisms with loading regimes (Bellini  
25  
26 and Güçeri 2003, Moroni, De Wijn et al. 2006, Lanzotti, Grasso et al. 2015). The effects of the  
27  
28 infill orientation have been previously discussed by other authors; these orientation arrangements  
29  
30 include unidirectional bead lay-up and criss-cross bead lay-up in which the beads of adjacent layers  
31  
32 are separated by  $90^\circ$  (Thomas and Renaud 2003). In both of these cases, the effect of the infill  
33  
34 orientation on the stiffness and strength of the component have been found similar to that of  
35  
36 composite materials (Rodríguez, Thomas et al. 2001). Nevertheless, the main difference between  
37  
38 3D printed parts and composite materials is the shear stress transfer mechanism among adjacent  
39  
40 layers. In the case of 3D printed components, adjacent beads, from a layer-upon-layer configuration  
41  
42 viewpoint, are blended rather than attached via a substrate material as typically encountered in  
43  
44 fibre-reinforced polymers. Therefore, the overlapping surface in 3D printed components could be  
45  
46 varied by modifying the parameters related to the deposition phase such as temperature, deposition  
47  
48 rate or contact pressure. The extension of bonding surfaces play an essential role for the 3D printed  
49  
50  
51  
52  
53  
54  
55  
56  
57  
58  
59  
60

1  
2  
3 parts, by withstanding the tangential load acting on the element while in long fibre-reinforced  
4 polymer composite, the shear performance is related to the strength of the matrix mainly.  
5  
6

7  
8 Attempts to adopt the interlaminar shear strength as a failure criterion for 3D printed parts have  
9  
10 been made by considering empirical coefficients to account for the effect of the overlapping  
11 surfaces (Thomas and Renaud 2003). However, inconsistencies continue to appear when comparing  
12 numerical results to experimental data of 3D printed parts (Bikas, Stavropoulos et al. 2016). In  
13 many cases, strength and stiffness of 3D printed parts have been investigated under simplistic  
14 conditions such as static loads at ambient temperature while neglecting the effect of time and  
15 temperature associated with the deposition period of the final part. Noteworthy, PLA undergoes  
16 physical changes during printing and whilst in service due to varying temperatures, namely glass  
17 transition, between 50°C and 70°C (Senatov, Niaza et al. 2016) and other thermal transitions.  
18  
19  
20  
21  
22  
23  
24

25  
26 Therefore this is a critical factor that must be considered in the production and use of PLA in a  
27 variety of applications within aerospace, automotive and medical sectors. AM implementation has  
28 seen a significant market growth over the last decade in several industries and research sectors. The  
29 market value of 3D printed components in the automotive sector ranked as the highest globally, has  
30 been estimated at 7000 million US dollars by 2025 while the medical applications sector is listed as  
31 the third fastest growing industry utilising such technologies (Feng, Wu et al. 2014). Despite the  
32 rapid growth in the number of AM-related publications over the last five years, approximately 3500  
33 per year, there is still a gap in the open literature regarding the effect of temperature on the  
34 mechanical properties of 3D printed components. Furthermore, in-situ mechanical testing over a  
35 range of in-service temperatures is a significant factor in identifying failure modes, that is, whether  
36 the fracture is brittle or ductile. Considering the viscoelastic nature of polymeric materials, the  
37 elastic proportion of stress-strain curve followed by a sudden drop in stress with no further  
38 extension is said to be a brittle fracture failure. However, in ductile dominant failure, the elastic and  
39 plastic proportion are merged with a decreased value of maximum stress and a prolonged extension  
40  
41  
42  
43  
44  
45  
46  
47  
48  
49  
50  
51  
52  
53  
54  
55  
56  
57  
58  
59  
60

1  
2  
3 which is sometimes infinite. These effects are controlled by the addition of plasticizers or  
4 temperature variation (Kendall and Siviour 2014). Therefore, it stands as mandatory to investigate  
5  
6 the impact of temperature on the strength and stiffness of the 3D printed materials; ultimately  
7  
8 benefiting the selection of 3D printing processing parameters or conditions, rather than just being a  
9  
10 geometric specification, according to the required applications.  
11  
12

13  
14 In this work, the thermal, mechanical properties of 3D printed PLA specimens has been investigated  
15  
16 by considering different raster angles and environmental temperatures 20°C- 60°C. The heat-  
17  
18 induced variations of the feeding material have also been studied by performing mechanical tests  
19  
20 on the plain, referring to the filaments before the extrusion process takes place, and the extruded  
21  
22 filaments in tensile mode configuration. This was done with the aim of assessing potential property  
23  
24 changes related to the physical variation of the polymeric material. Thus, the ultimate tensile  
25  
26 strength, Young's modulus, strain at failure and stress at failure of these 3D-printed samples were  
27  
28 determined at different temperatures to evaluate final material performance along three bead  
29  
30 orientations, namely 0o/90o, -30/60o, ±45o, while the temperature was kept constant over several  
31  
32 values ranging between 20°C and 60°C.  
33  
34

## 35 2. Materials and Methods

### 36 2.1. PLA Filament Sample Preparation and Mechanical Characterisation

37  
38 In order to assess the potential physical change in the feeding material due to the time-temperature  
39  
40 profile undergone by the system during the deposition stage, preliminary mechanical tests were  
41  
42 carried out on plain and on freely extruded PLA filament samples, that is those that are left to run  
43  
44 for a few seconds as part of the filament loading process and cleared from the build plate before  
45  
46 printing takes place. Each test was repeated five times for statistical significance. In Table 1, the  
47  
48 plain and freely extruded wire-like samples are reported along with the considered temperatures  
49  
50 and the number of performed test repetitions.  
51  
52

Table 1 - Experimental plan for the PLA filament

FILAMENT	T (°C)	REPETITIONS
EXTRUDED PLA FILAMENT	20-30-40-50-60	5

PLA filaments, both plain and extruded, were tested by using a Dynamic Mechanical Analyser, model Q800 DMA (TA Instruments Italy), equipped with a fibre tension clamp. The tension tests were force controlled up to the maximum 18 N by using a force ramp of 1 N/min. Nominal dimensions of the cylindrical wire-like filament were 15 mm in length and 1.75 mm and 0.60 mm in diameter for plain and extruded filaments respectively.

## 2.2. PLA Standard Specimen Preparation and Testing

Tensile mechanical tests were carried out on standard PLA 3D-printed samples (see Figure 1) to characterise specimens with three different bead orientations, namely 0°, 90°, -30°, 60° and ±45°, over a range of different temperatures from room temperature (20°C) to 60°C with a step increment of 10°C. To avoid the failure of the specimens outside the gauge length, likely brought about by the approximation of curvatures as a result of the discretised geometry produced at the termination FDM roads, the geometry proposed in (Lanzotti, Grasso et al. 2015) was adopted. In particular, this geometry has a fillet with a parabolic curve drawn as an arc (with a radius of 1,000 mm) tangent to the start of the linear segment at the reduced section of the specimen. Specimen dimensions are specified in Figure 1.

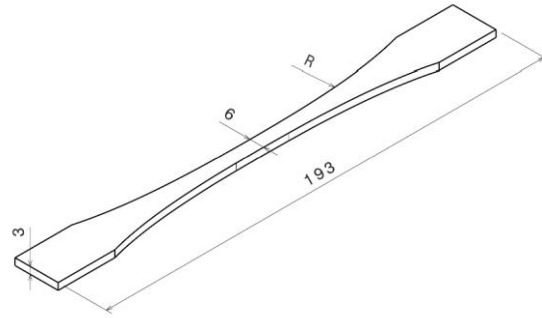


Figure 1 – Standard sample nominal dimensions. All dimension in millimetres.

As reported by (Ahn, Montero et al. 2002) this geometry reduces premature shear failure at the stress concentrations caused by the discretization of large radii along the length of the specimen; this is particularly evidenced at the termination of FDM roads or insets to approximate large radii. The geometry of the 3D samples and the stereolithographic (STL) files were generated with the CAD software CATIA V5 (Dassault Systemes, Velizy-Villacoublay, France). As illustrated in Figure 2, the specimens were printed in the x-y plane and rotated about the z-axis with a raster angle of  $0^\circ$ ,  $30^\circ$  and  $45^\circ$  to generate the different infill orientations  $0^\circ/90^\circ$ ,  $-30^\circ/60^\circ$  and  $\pm 45^\circ$  respectively; see Figure 3.

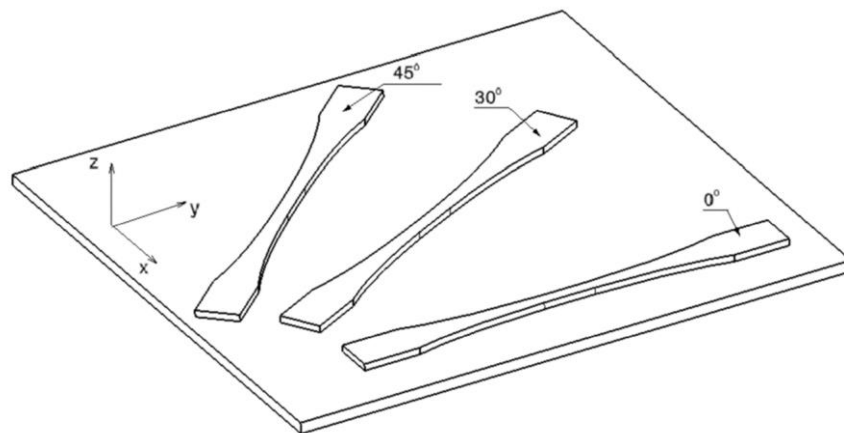


Figure 2 - Schematic arrangement of the different raster angle values ( $0^\circ - 30^\circ - 45^\circ$ ) adopted to print the three different infill orientations



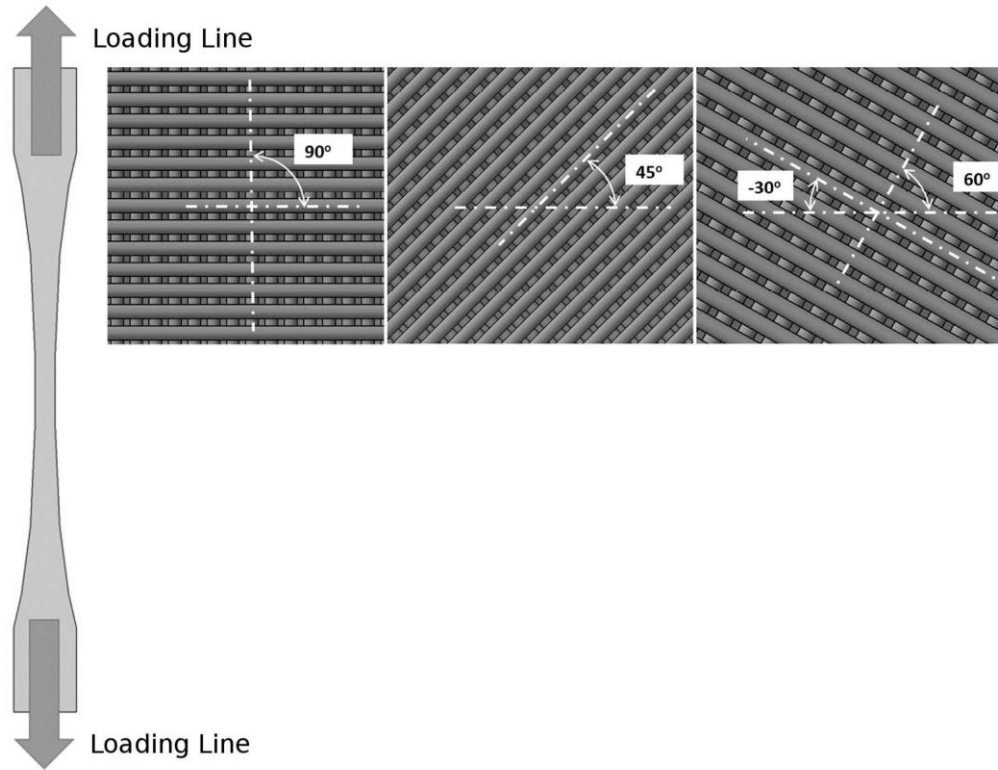


Figure 3 Schematic representation of the three different infill orientations

A total of 75 standard tensile specimens were produced and tested, within which, each of the three different infill orientations was tested at five different temperatures from 20 to 60 °C. The tensile tests were repeated five times to ensure statistical significance. Table 2 reports the experimental plan for all PLA samples manufactured at different infill orientations and temperatures. The ID indicated in Table 2 is composed of two parts; the first signifies the temperature value (T1, T2 and T3) and the second signifies the considered orientation (O1, O2 and O3).

Table 2 Experimental plan

ID	INFILL ORIENTATION	T (°C)	REPETITIONS
T2O1	0°/90°	30	5

<b>T301</b>	0°/90°	40	5
<b>T401</b>	0°/90°	50	5
<b>T501</b>	0°/90°	60	5
<b>T102</b>	-30°/60°	20	5
<b>T202</b>	-30°/60°	30	5
<b>T302</b>	-30°/60°	40	5
<b>T402</b>	-30°/60°	50	5
<b>T502</b>	-30°/60°	60	5
<b>T103</b>	±45°	20	5
<b>T203</b>	±45°	30	5
<b>T303</b>	±45°	40	5
<b>T403</b>	±45°	50	5
<b>T503</b>	±45°	60	5

The MakerBot Replicator Desktop 3D printer (MakerBot Industries, Brooklyn, USA) with a 0.4-mm diameter nozzle was used to produce the tensile test specimens. The values of the primary geometry control parameters including layer thickness, number of shells or perimeters and overlapping are shown in Table 3. The aforementioned parameters, together with the printing process parameters such as feed rate, travel speed and print temperature, were tuned. This tuning was based on the quality of the print out specimens in terms of dimensions, smoothness of the outer surfaces and the volume of material needed to print the samples.

*Table 3 Printing parameters implemented in the MakerBot Replicator*

<b>Parameters</b>	<b>Value</b>	<b>Unit</b>
<b>Layer height</b>	<b>0.18</b>	<b>mm</b>
<b>Infill Layer Height</b>	<b>0.18</b>	<b>mm</b>
<b>Number of shells</b>	<b>2</b>	<b>-</b>
<b>Feed rate</b>	<b>1</b>	<b>mm/s</b>
<b>Travel feed rate</b>	<b>10</b>	<b>mm/s</b>
<b>Print temperature</b>	<b>215</b>	<b>°C</b>
<b>Filament diameter</b>	<b>1.75</b>	<b>mm</b>

<b>Nozzle diameter</b>	<b>0.4</b>	<b>mm</b>
<b>Infill Density</b>	<b>40 %</b>	<b>-</b>
<b>Floor Thickness</b>	<b>1.5</b>	<b>mm</b>
<b>Support Angle</b>	<b>68o</b>	<b>-</b>
<b>Support Density</b>	<b>20 %</b>	<b>-</b>
<b>Cooling Fan Speed</b>	<b>50 %</b>	<b>-</b>
<b>Infill Pattern</b>	<b>Linear</b>	<b>-</b>

The tensile tests were performed using an Instron electromechanical testing machine D3367 Dual Column System (Instron, United Kingdom) equipped with Bluehill software (Instron, United Kingdom). The load was measured with a 30 kN load cell having an accuracy of  $\pm 0.5\%$ . Each specimen was clamped to the electromechanical testing machine at a specified grip separation of 150 mm and loaded along the longitudinal axis with a cross-head speed of 2 mm/min to failure. The temperature was controlled by an Instron environmental chamber 3119-610 (Instron, United Kingdom). In addition, the temperature of each specimen was also monitored by means of an infrared (IR) camera FLIR TG165 (FLIR Systems, United States) which identifies the temperature distribution in the gage length of each tested specimen. In Figure 4, the gage length of one of the samples tested at 60°C is shown. In this Figure, it is possible to see the uniform temperature distribution over the central part of the specimen and a temperature value that differs from the nominal value by  $\pm 1^\circ$ . Although, the temperature displayed on the IR camera is accurate enough on the surface of the specimens, there are some limitations regarding the identification of the temperature profile throughout the thickness of the samples.

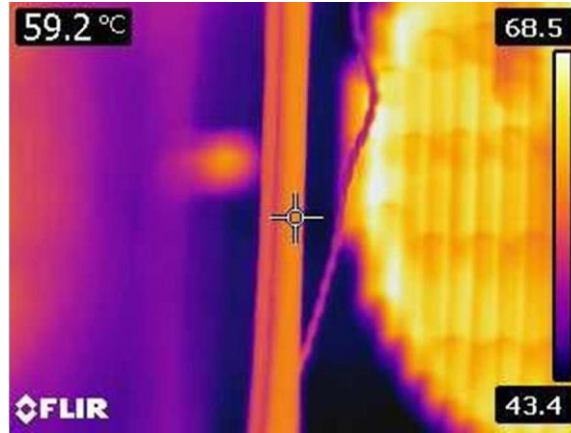


Figure 4 - Temperature contour plot acquired with the IR camera

A preconditioning procedure to record the time needed to reach a specified temperature was carried out. Samples were heated from room temperature to the desired temperature value and the time for each temperature increment was recorded. These times were found to be 3, 7, 10 and 15 minutes at the given temperatures of 30°C, 40°C, 50°C and 60°C respectively.

A Load-displacement curve was acquired during each test which was analysed and later converted into the stress-strain curve. The applied stress was computed as the ratio between the applied load and the initial minimum cross-section area, while the strain was derived by dividing the cross-head displacement over the initial gripping length of the specimen (150 mm). It is worth mentioning that the calculated minimum cross-section area was based on the externally measured dimensions. However, the potential voids within the built structure are not accounted for in this calculation. The average values of the mechanical properties with the corresponding standard deviation have been computed for each group of 5 specimens considered at a given orientation and temperature. The ultimate tensile strength (UTS), Young's modulus (E), the stress at failure and the strain at failure have been derived in accordance with ASTM: D638 Standard.

Due to the lack in the current literature regarding the effects of the temperature on PLA 3D printed component, it was decided to narrow-down the investigation and focus the attention on the

1  
2  
3 combined effect of the infill orientation and the temperature values, while fixing the other  
4 parameters.  
5  
6  
7  
8  
9

### 10 **2.3 Fractography Analysis of 3D printed specimen**

11 Fracture surfaces of the tensile test specimens were examined using a LEICA DFC295 digital  
12 microscope colour camera (Leica Microsystems, United Kingdom) with a resolution of 2048x1536  
13 pixels (3 Megapixels). The fracture surfaces contain necking as well as voids due to the printing  
14 imperfection and the fracture process itself. The fracture surfaces were scanned for these features  
15 and as a way of confirming the nature of the failure mechanism. The microscopic observations of  
16 the samples tested at different temperature values highlighted porosity due to the printing process  
17 as well as the variation in necking. The specimens examined at 50°C and 60°C did not reach  
18 complete separation and were therefore not analysed.  
19  
20  
21  
22  
23  
24  
25  
26  
27  
28

## 29 **3. Results and discussion**

### 30 **3.1 Filaments**

31 Tensile tests were carried out on the PLA filament before and after printing. The average curves  
32 obtained from the tests performed at the four different temperature values (30°C, 40°C, 50°C,  
33 60°C) are reported in Figure 5. Apart from the highest temperature test (60°C) which did not fail,  
34 the remaining specimens failed after their nominal extension had been recorded.  
35  
36  
37  
38  
39  
40  
41  
42  
43  
44  
45  
46  
47  
48  
49  
50  
51  
52  
53  
54  
55  
56  
57  
58  
59  
60



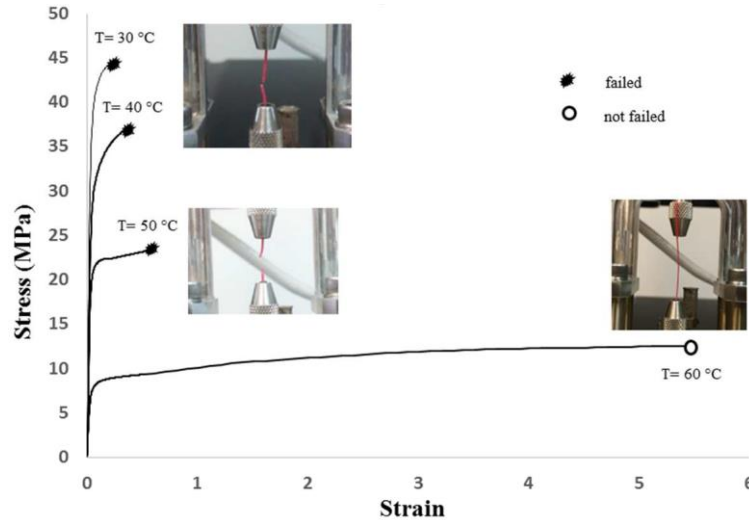


Figure 5 Stress vs strain for printed PLA curve: tensile strength decreased while strain increased as temperature increases

As expected, increasing the temperature results in a significant higher strain at failure. As the temperature increases, the molecular segments motion is triggered enabling free chain movement up to the glass transition phase ( $\sim 60^{\circ}\text{C}$ ) which explains the continuous extension of the filament without a defined failure point (Saeidlou, Huneault et al. 2012). Ductile polymers tend to have a well-defined yield point with high strain typically of the order 5-10 % due to their semicrystalline state, whereas most amorphous glassy polymers are typically brittle and rupture at definite low strains.. These effects are generally controlled by the addition of plasticisers or temperature variation (Kendall and Siviour 2014).

Table 3 Experimental result for neat and printed filaments from the tensile test.

TEMPERATURE	YOUNG MODULUS [MPA]	
	NEAT PLA	3D-PRINTED PLA
30°C	1175±89	<b>1400±78</b>
40°C	1011±75	<b>1143±82</b>
50°C	701±54	<b>961±54</b>
60°C	<b>247±16</b>	<b>350±12</b>

1  
2  
3 Results reported in Table 3 reveal that the thermal history undergone by the polymer during the  
4 deposition phase will affect inherently the mechanical property of the final fused (printed) polymer.  
5  
6

7  
8 For this reason, a modelling approach should take into account the variations on the mechanical  
9 properties, from the original feeding material, induced by the printing operations.  
10

11 According to the tensile stiffness recorded for both plain and 3D printed PLA, it can be observed  
12 that there is an inverse relationship between temperature increase and modulus reduction. However,  
13 it is worthwhile to mention the comparable reduction in stiffness from 30% in plain PLA to 16%  
14 for the freely extruded filaments as the temperature increases from 40°C to 50°C. This can be  
15 explained by the cold crystallisation effects of such polymers and molecular chain re-alignment  
16 along the testing direction (Martin and Avérous 2001). The thermal dependence of PLA properties  
17 is explained by the direct influence of its thermal history on the crystallinity of PLA (Farah,  
18 Anderson et al. 2016). Therefore, the melting process, within the nozzle, during 3D printing results  
19 in the  $\alpha$  growth of PLA crystals (Farah, Anderson et al. 2016). The dramatic drop in stiffness as the  
20 temperature approaches the glass transition 60°C, is associated with the glass transition of the  
21 polymer into a semi-liquid or rubbery state. This phase is characterised by the expanded free  
22 volume which promotes free particles movement and consequently reduces the interlocking  
23 mechanism; hence, lowering the measured stiffness (Nikzad, Masood et al. 2011).  
24  
25  
26  
27  
28  
29  
30  
31  
32  
33  
34  
35  
36  
37

### 38 39 **3.2 3D printed specimens**

40  
41 Tensile tests carried out on the 3D printed specimens by means of the electromechanical INSTRON  
42 machine, for each group the average over the five values acquired together with the standard  
43 deviation is reported. In correspondence to temperature values 50°C and 60°C; the transition in the  
44 mechanical behaviour due to the  $T_g$  changes the constraint of the polymeric chains allowing them  
45 to move and slide under the action of the applied load. This condition results in a continuous  
46 elongation under a constant applied load. Since the failure condition is not reached, the tensile test  
47  
48  
49  
50  
51  
52  
53  
54  
55  
56  
57  
58  
59  
60



1  
2  
3 was stopped once a strain of 0.2% was reached. It has been assumed that this elongation  
4 corresponds to the condition for which the functionality of the component is lost, even if separation  
5  
6  
7  
8 is not accomplished.  
9

10 The results presented in Figure 6 indicates the strong influence of temperature increase on both  
11 stiffness and ultimate strength UTS of the FDM specimen. It can be clearly observed that as the  
12 temperature increases the stiffness and UTS decrease. At temperatures below 40°C, the stiffness  
13 values fluctuate within a narrow range before plummeting at temperatures of 50°C and 60°C due to  
14 the glass transition. However, UTS values experienced a gradual decrease with respect to  
15 temperature increase up to 50°C at which point a dramatic fall in strength is recorded and continues  
16 to drop at 60°C.  
17  
18  
19  
20  
21  
22

23 The results acquired at room temperature through tensile tests have confirmed the well-known  
24 dependency of the stiffness and strength on the infill orientation (Lanzotti, Grasso et al. 2015).  
25 According to the current literature, the maximum value of Young's modulus (E) at room  
26 temperature was found in correspondence of  $\pm 45^\circ$  orientation. This is different to the observed  
27 trend found in polypropylene specimens in (Carneiro, Silva et al. 2015) in which the maximum  
28 Young's modulus (E) occurred at  $0^\circ/90^\circ$  orientation. The same response is observed when  
29 considering the strength measured as UTS. These observations agree well with the results reported  
30 by Dawoud et al., (Dawoud, Taha et al. 2016) in which the tensile strength of ABS, at  $\pm 45^\circ$   
31 orientation was consistently higher than other orientations used in the study for both positive and  
32 negative air gap. However, another study on the influence of build parameters of PEEK samples by  
33 (Wu, Geng et al. 2015) on the mechanical properties revealed contradicting results to those reported  
34 by Dawoud as the maximum strength was recorded for the  $0^\circ/90^\circ$  orientation.  
35  
36  
37  
38  
39  
40  
41  
42  
43  
44  
45  
46  
47  
48  
49  
50  
51  
52  
53  
54  
55  
56  
57  
58  
59  
60

1  
2  
3  
4  
5  
6  
7  
8  
9  
10  
11  
12  
13  
14  
15  
16  
17  
18  
19  
20

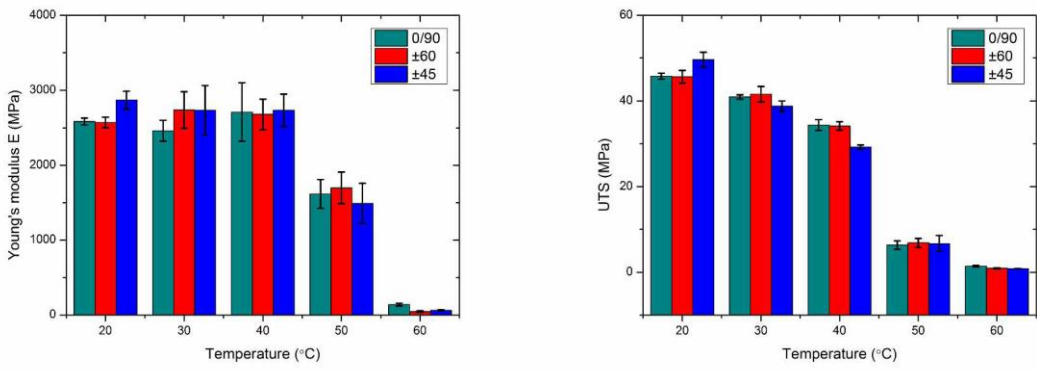
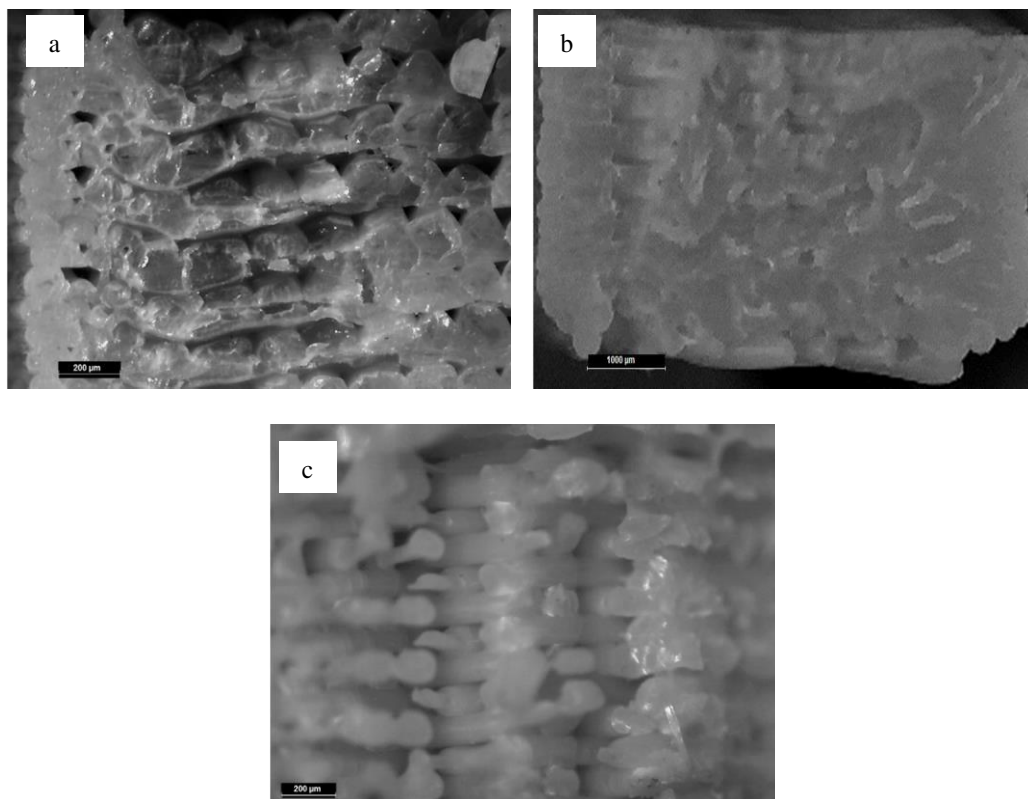


Figure 6 - Young's Modulus (left) and UTS (right) comparison for different infill orientation as temperature increases.

23  
24  
25  
26  
27  
28  
29  
30  
31  
32  
33  
34  
35  
36  
37  
38  
39  
40  
41  
42  
43  
44  
45  
46  
47  
48  
49  
50  
51  
52  
53  
54  
55  
56  
57  
58  
59  
60

1  
2  
3 The difference in the average values of Young's modulus ( $E$ ) between  $0^\circ/90^\circ$  and  $30^\circ/60^\circ$  is 12  
4 MPa. For  $0^\circ/90^\circ$  the axial load is taken partially by half of the layers oriented along the loading  
5 direction and partially by the rest of the layers oriented along the orthogonal direction. The  
6 contribution of the latter in sustaining the load is limited to the bonding surfaces that are weaker  
7 than the beads. However, the deformability of the cross section is limited hence the brittle failure is  
8 dominant as shown in Figure 7a. The irregular shape of the beads, as well as the bonding region  
9 between beads, as well as the bonding region between beads locally increases the stress promoting  
10 failure. As already described by (Durgun and Ertan 2014), the failure mode is a result of the  
11 material separation in a plane approximately normal to the tensile stress. The failure is caused by  
12 pulling with high tensile strength and eventual rupture, as the tensile loads were taken by beads  
13 themselves.  
14  
15  
16  
17  
18  
19  
20  
21  
22  
23  
24  
25 themselves.



53 *Figure 7 - Microscopic images of specimens printed at: a)  $0^\circ/90^\circ$ , b)  $-30^\circ/60^\circ$  and c)  $\pm 45^\circ$  after testing at*  
54  
55  
56  
57  
58  
59  
60

20°C.

When the beads are oriented along  $-30^{\circ}/60^{\circ}$  in each layer the axial load has a component along the direction of the beads. As seen in Figure 7b the presence of more beads that withstand the load compensate the less part of the load taken by the more extended bonding surfaces resulting in a limited reduction of the stiffness value. When the beads are oriented along  $\pm 45^{\circ}$ , the diamond arrangement of the oriented beads (Figure 7c) enables the increased load taken with minimal extension compared to the two previous orientations, having at the same time a lower extension of the bonding surfaces. Regarding the strength, the minimum UTS value is reached at  $-30^{\circ}/60^{\circ}$  due to the fact that the bonding surfaces play a crucial role in reducing the load sustained by the specimen. At 40 °C the minimum value of the stiffness is reached at  $-30^{\circ}/60^{\circ}$  and the maximum at  $\pm 45^{\circ}$  with a difference between  $\pm 45^{\circ}$  and  $0^{\circ}/90^{\circ}$  of 26 MPa. The minimum value of the UTS is reached at  $\pm 45^{\circ}$  and the maximum at  $0^{\circ}/90^{\circ}$ . The higher stiffness value at  $\pm 45^{\circ}$  corresponds to a lesser value of the strength with the minimum value of the UTS. For all other orientations, necking plays a major role in the failure mechanism resulting in an immediate failure after the UTS is reached. The tests carried out at 40°C have shown a failure mode mainly ductile with necking in the beads and visible necking in the cross-section of the specimens.

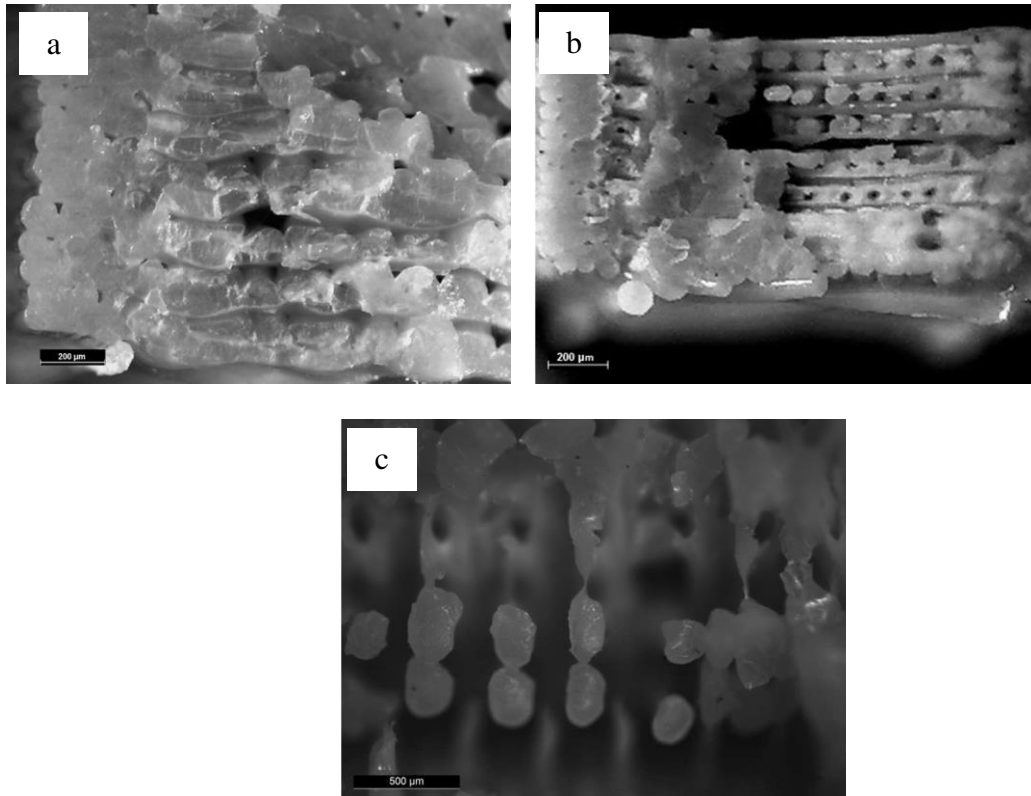


Figure 8 - Microscopic images of specimens printed at: a)  $0^{\circ}/90^{\circ}$ , b)  $-30^{\circ}/60^{\circ}$  and c)  $\pm 45^{\circ}$  after testing at  $40^{\circ}\text{C}$ .

The combination of infill orientation and temperature results in the failure of the beads. The combination of infill orientation and temperature trigger the shear failure of the samples. Shear is induced by the force acting in parallel planes, consequently sliding movement of beads layers along the build direction as depicted in Figure 9. Bonding surfaces are the contact regions created among adjacent beads. In fact, when all beads are broken, the load is carried mainly by the bonding surfaces which will tend to creep along their directional planes due to shear forces. Moreover, the inspection of the fracture surfaces (Figures 8 a,b and c) of the specimens together with the analysis of the stress-strain curves reveal that the response is characterized by evident softening due to the shear response resulting in a higher strain at failure. The effects of the temperature promote creep which contributes to the greater elongation (Yang, Zhang et al. 2006).

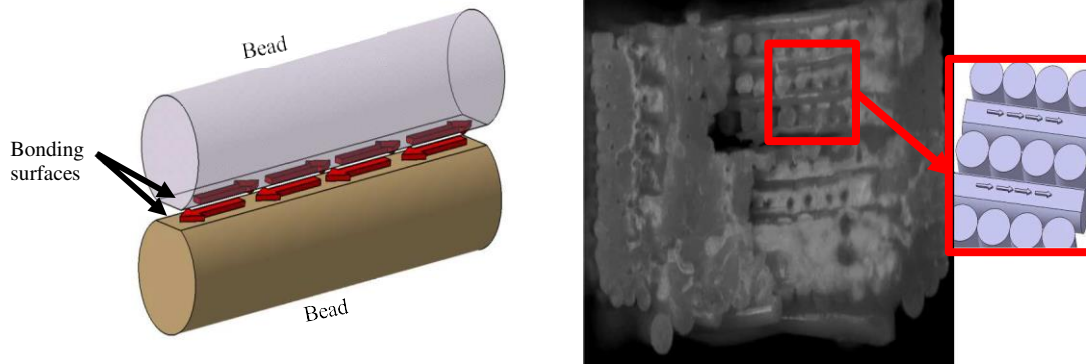


Figure 9 Sliding movement of bonding surfaces under shear stress (left), visual and representative

At 50°C there is a drop in the stiffness values for 0°/90° and ±45° which are 1100 MPa and 1250 MPa respectively. At 50 °C, the effect of temperature on the -30°/60° is different due to the different contribution from the beads and the bonding surfaces. In this particular case, most of the beads are oriented closer to the loading line resulting in most of the load being taken by the beads rather than the bonding surfaces.

At 60°C, a value that is greater than the  $T_g$ , the values for Young's modulus (E) are considerably low for all considered orientations. Below this temperature, any dimensional changes are dominated by the temporary distortions of the primary valence bonds. As polymers are either semi-crystalline or amorphous, the resulted structure after extrusion is considered to be in the semicrystalline phase, with repeating crystals, which is responsible for the higher tensile strength and stiffness. These properties decrease drastically above the  $T_g$  (Van de Velde and Kiekens 2002). However, it is still possible to identify the difference between the three orientations, and in particular, the maximum value is reached at 0°/90° whilst the minimum at -30°/60°.

Regarding stress at failure, the maximum value at room temperature was recorded at 0°/90° while the minimum occurred at ±45°. A general trend is observed in Figure 10, increasing the temperature value causes reduction of the stress at failure for the 0°/90° and -30°/60°. As observed with the optical

microscope in Figure 8c, the extended necking, plastic deformation and the brittleness of the bonding surfaces, which are playing a predominant role for this orientation, are affecting the beads as well as the entire cross-section. On the other hand, for the other two orientations the contribution from the beads is predominant compared to the bonding surfaces, and consequently, the stress at failure is much higher. For the tests carried out at 50°C and 60°C, the stress of failure is identified as the constant stress under which the material flow at high strain values.

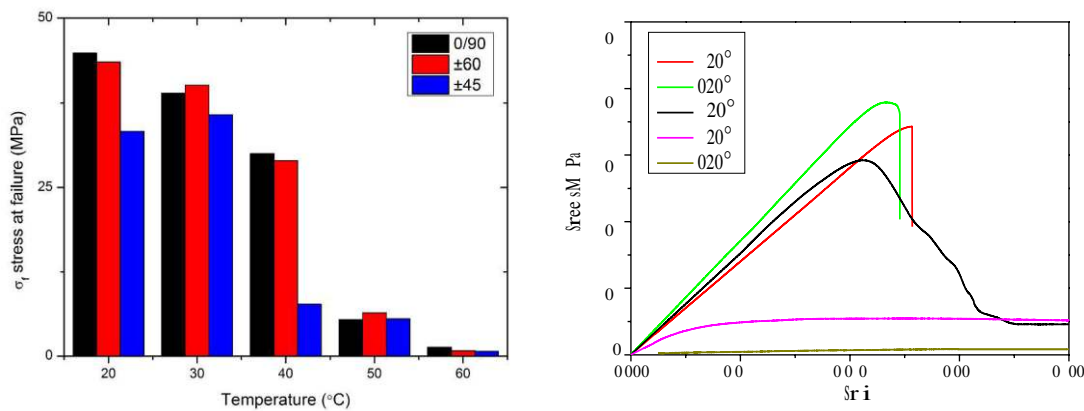


Figure 10 Stress at failure as a function of temperature (left): stress at failure decreases as temperature increases for all infill orientations, Stress vs strain curves of  $\pm 45^\circ$  samples (right)

The strain at failure at 50°C and 60°C were evaluated at 0.2% since failure with the complete separation of the two ends of the sample was never reached. For that reason, it is not possible to make any comparisons. At room temperature, the maximum strain at failure is reached at  $\pm 60^\circ$  as the overall longitudinal strain is mainly composed by the elongation of the beads along the loading line. The lowest strain at failure at 20°C occurs at  $\pm 45^\circ$ , since the strain is mostly contributed by the bonding surfaces without any significant axial elongation of the beads.

As the temperature increases to 40°C, the highest strain at failure value is reached at  $\pm 45^\circ$  whereas the lowest value is at  $\pm 60^\circ$ . The combination of bonding surfaces deformation with the

axial elongation of the beads can also explain the different behaviour at that temperature value. The increase in temperature is causing a drop in the shear strength of the bonding surface among beads. As a result, the load is mainly carried by the beads since the resistance opposed by the bonding surfaces is minimal. The more load carried by the beads results in more elongation and a dominant necking all over the cross-section.

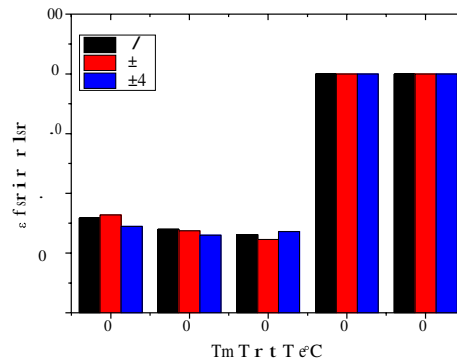


Figure 11 Strain at failure for different infill orientations as a function of temperature

#### 4. Conclusion

In this paper, the effects of the temperature on the mechanical response of PLA 3D printed specimens was studied. The standard process parameters were changed to identify the correlations between the printing parameters and the temperature values. The response surfaces were used to derive the required relationship among process parameters, temperature, the tensile stiffness, the UTS, the strain and stress at failure. The analysis of the experimental results made it possible to understand the impact of control factors on the mechanical properties of specimens produced using the Fusion Additive Manufacturing. The tensile tests carried out on single filaments before and after the extrusion process with the 3D printer have shown a reduction in stiffness from 30% in plain PLA filaments to 16% in 3D printed filament as temperature increases from 40 °C to 50 °C. This was explained by the cold crystallisation effects of such polymers and molecular chain re-alignment along the testing direction. Furthermore, the results of the tensile tests carried out on the



1  
2  
3 3D printed samples at different temperature values were reported and discussed. With regard to  
4  
5  
6 Young's modulus (E) values, it is possible to observe a common trend for  $0^\circ/90^\circ$  and  $\pm 45^\circ$  as the  
7  
8 temperature increases, while for  $-30^\circ/60^\circ$  at  $50^\circ\text{C}$  it is following a different path presenting a  
9  
10 higher magnitude when compared to the other two orientations. Regarding the UTS, it is  
11  
12 possible to identify a continuous reduction in values as the temperature increases and the three  
13  
14 configurations follow the same path. The stress at failure for the  $\pm 45^\circ$  orientation is showing a  
15  
16 peculiar phenomenon with the maximum value at  $30^\circ\text{C}$  and a sudden drop at  $40^\circ\text{C}$ ; this latter is  
17  
18 higher than what was observed for the other two orientations. At  $\pm 45^\circ$ , the temperature  
19  
20 variation from  $20^\circ\text{C}$  to  $30^\circ\text{C}$  lowers the strength of the bonding surface which is counterbalanced  
21  
22 by the beads robustness into the overall force loading balance of the sample. At a higher  
23  
24 temperature, however, closer to the glass transition temperature of the PLA, (i.e.  $40^\circ\text{C}$ ), the  
25  
26 weakness of the beads induces a redistribution of the stresses to determine a magnitude level at  
27  
28 bonding surface which exceeds the shear strength of the interface determine the failure. For  $0^\circ/90^\circ$   
29  
30 and  $-30^\circ/60^\circ$  the stress at failure decrease as the temperature increases with a consistent reduction  
31  
32 at  $50^\circ\text{C}$  which is close to the  $T_g$  for PLA. Regarding the strain at failure, it was observed that  
33  
34 the combination of bonding surfaces deformation with the axial elongation of the beads can  
35  
36 explain the different behaviours of the three orientations here investigated as the temperature  
37  
38 values increase. There is potential for further analyses of the thermomechanical properties of  
39  
40 FDM parts using finite element analysis methods to model the material properties based on the  
41  
42 experimental stress-strain results.  
43  
44  
45  
46  
47  
48  
49

## 50 **References**

51  
52 Ahn, S.-H., M. Montero, D. Odell, S. Roundy and P. K. Wright (2002). "Anisotropic  
53  
54 material properties of fused deposition modeling ABS." Rapid prototyping journal **8**(4):  
55  
56  
57  
58  
59  
60

1  
2  
3 248-257.

4 Bellini, A. and S. Güçeri (2003). "Mechanical characterization of parts fabricated using  
5 fused deposition modeling." Rapid Prototyping Journal **9**(4): 252-264.  
6  
7

8  
9 Bikas, H., P. Stavropoulos and G. Chryssolouris (2016). "Additive manufacturing methods  
10 and modelling approaches: a critical review." The International Journal of Advanced  
11 Manufacturing Technology **83**(1-4): 389-405.  
12

13  
14 Bito, J., R. Bahr, J. G. Hester, S. A. Nauroze, A. Georgiadis and M. M. Tentzeris (2017).  
15 "A Novel Solar and Electromagnetic Energy Harvesting System With a 3-D Printed  
16 Package for Energy Efficient Internet-of-Things Wireless Sensors." IEEE Transactions on  
17 Microwave Theory and Techniques.  
18

19  
20 Carneiro, O. S., A. F. Silva and R. Gomes (2015). "Fused deposition modeling with  
21 polypropylene." Materials & Design **83**: 768-776.  
22

23  
24 Dawoud, M., I. Taha and S. J. Ebeid (2016). "Mechanical behaviour of ABS: An  
25 experimental study using FDM and injection moulding techniques." Journal of  
26 Manufacturing Processes **21**: 39-45.  
27

28  
29 de Obaldia, E. E., C. Jeong, L. K. Grunenfelder, D. Kisailus and P. Zavattieri (2015).  
30 "Analysis of the mechanical response of biomimetic materials with highly oriented  
31 microstructures through 3D printing, mechanical testing and modeling." Journal of the  
32 mechanical behavior of biomedical materials **48**: 70-85.  
33

34  
35 Durgun, I. and R. Ertan (2014). "Experimental investigation of FDM process for  
36 improvement of mechanical properties and production cost." Rapid Prototyping Journal  
37 **20**(3): 228-235.  
38

39  
40 Farah, S., D. G. Anderson and R. Langer (2016). "Physical and mechanical properties of  
41 PLA, and their functions in widespread applications — A comprehensive review."  
42 Advanced Drug Delivery Reviews **107**: 367-392.  
43  
44

45  
46 Feng, S., D. Wu, H. Liu, C. Chen, J. Liu, Z. Yao, J. Xu and M. Zhang (2014).  
47 "Crystallization and creep of the graphite nanosheets based poly(butylene adipate-co-  
48 terephthalate) biocomposites." Thermochimica Acta **587**(Supplement C): 72-80.  
49

50  
51 Gibson, I., D. W. Rosen and B. Stucker (2010). Additive manufacturing technologies,  
52 Springer.  
53  
54

- 1  
2  
3 Hong, A. L., B. T. Newman, A. Khalid, O. M. Teter, E. A. Kobe, M. Shukurova, R.  
4 Shinde, D. Sipzner, R. J. Pignolo and J. K. Udupa (2017). Feasibility of fabricating  
5 personalized 3D-printed bone grafts guided by high-resolution imaging. SPIE Medical  
6 Imaging, International Society for Optics and Photonics.  
7  
8  
9 Impens, D. and R. Urbanic (2016). "A comprehensive assessment on the impact of post-  
10 processing variables on tensile, compressive and bending characteristics for 3D printed  
11 components." Rapid Prototyping Journal **22**(3): 591-608.  
12  
13  
14 Keles, O., C. W. Blevins and K. J. Bowman (2017). "Effect of build orientation on the  
15 mechanical reliability of 3D printed ABS." Rapid Prototyping Journal **23**(2).  
16  
17  
18 Kendall, M. J. and C. R. Siviour (2014). Rate dependence of poly (vinyl chloride), the  
19 effects of plasticizer and time-temperature superposition. Proc. R. Soc. A, The Royal  
20 Society.  
21  
22  
23 Lanzotti, A., M. Grasso, G. Staiano and M. Martorelli (2015). "The impact of process  
24 parameters on mechanical properties of parts fabricated in PLA with an open-source 3-D  
25 printer." Rapid Prototyping Journal **21**(5): 604-617.  
26  
27  
28 Li, J., B. Wu and C. Myant (2016). "The Current Landscape for Additive Manufacturing  
29 Research."  
30  
31  
32 Martin, O. and L. Avérous (2001). "Poly(lactic acid): plasticization and properties of  
33 biodegradable multiphase systems." Polymer **42**(14): 6209-6219.  
34  
35  
36 Moroni, L., J. De Wijn and C. Van Blitterswijk (2006). "3D fiber-deposited scaffolds for  
37 tissue engineering: influence of pores geometry and architecture on dynamic mechanical  
38 properties." Biomaterials **27**(7): 974-985.  
39  
40  
41 Nikzad, M., S. Masood and I. Sbarski (2011). "Thermo-mechanical properties of a highly  
42 filled polymeric composites for fused deposition modeling." Materials & Design **32**(6):  
43 3448-3456.  
44  
45  
46 Qin, Z., B. G. Compton, J. A. Lewis and M. J. Buehler (2015). "Structural optimization of  
47 3D-printed synthetic spider webs for high strength." Nature communications **6**.  
48  
49  
50 Rodríguez, J. F., J. P. Thomas and J. E. Renaud (2001). "Mechanical behavior of  
51 acrylonitrile butadiene styrene (ABS) fused deposition materials. Experimental  
52 investigation." Rapid Prototyping Journal **7**(3): 148-158.  
53  
54  
55  
56  
57  
58  
59  
60

1  
2  
3 Saeidlou, S., M. A. Huneault, H. Li and C. B. Park (2012). "Poly(lactic acid)  
4 crystallization." Progress in Polymer Science **37**(12): 1657-1677.

6 Senatov, F., K. Niaza, M. Y. Zadorozhnyy, A. Maksimkin, S. Kaloshkin and Y. Estrin  
7 (2016). "Mechanical properties and shape memory effect of 3D-printed PLA-based porous  
8 scaffolds." Journal of the mechanical behavior of biomedical materials **57**: 139-148.

10 Shakor, P., J. Sanjayan, A. Nazari and S. Nejadi (2017). "Modified 3D printed powder to  
11 cement-based material and mechanical properties of cement scaffold used in 3D printing."  
12 Construction and Building Materials **138**: 398-409.

14 Thomas, J. P. and J. E. Renaud (2003). "Design of fused-deposition ABS components for  
15 stiffness and strength." Journal of Mechanical Design: 545-551.

17 Torres, J., M. Cole, A. Owji, Z. DeMastry and A. P. Gordon (2016). "An approach for  
18 mechanical property optimization of fused deposition modeling with polylactic acid via  
19 design of experiments." Rapid Prototyping Journal **22**(2): 387-404.

21 Torres, J., J. Cotelos, J. Karl and A. P. Gordon (2015). "Mechanical Property Optimization  
22 of FDM PLA in Shear with Multiple Objectives." Jom **67**(5): 1183-1193.

23 Van de Velde, K. and P. Kiekens (2002). "Biopolymers: overview of several properties and  
24 consequences on their applications." Polymer Testing **21**(4): 433-442.

25 Visscher, D. O., E. J. Bos, M. Peeters, N. V. Kuzmin, M. L. Groot, M. N. Helder and P. P.  
26 van Zuijlen (2016). "Cartilage tissue engineering: Preventing tissue scaffold contraction  
27 using a 3D-printed polymeric cage." Tissue Engineering Part C: Methods **22**(6): 573-584.

28 Wu, W., P. Geng, G. Li, D. Zhao, H. Zhang and J. Zhao (2015). "Influence of layer  
29 thickness and raster angle on the mechanical properties of 3D-printed PEEK and a  
30 comparative mechanical study between PEEK and ABS." Materials **8**(9): 5834-5846.

31 Yang, J.-L., Z. Zhang, A. K. Schlarb and K. Friedrich (2006). "On the characterization of  
32 tensile creep resistance of polyamide 66 nanocomposites. Part I. Experimental results and  
33 general discussions." Polymer **47**(8): 2791-2801.